JACS
JOURNAL OF THE AMERICAN CHEMICAL SOCIETY
Article
pubs.acs.org/JACS

Ambient Scalable Synthesis of Surfactant-Free Thermoelectric CuAgSe Nanoparticles with Reversible Metallic-*n*-*p* Conductivity Transition

Chao Han,[†] Qiao Sun,[†,‡] Zhen Xiang Cheng,[†] Jian Li Wang,[†] Zhen Li,*[,†,‡] Gao Qing (Max) Lu,[§] and Shi Xue Dou[†]

[†]Institute for Superconducting and Electronic Materials, Australian Institute for Innovative Materials, University of Wollongong, Squires Way, North Wollongong, New South Wales 2500, Australia

[‡]School of Radiation Medicine and Radiation Protection, Soochow University, 199 Ren Ai Road, Suzhou Industrial Park, Suzhou 215123, China

[§]Australian Institute for Bioengineering & Nanotechnology, The University of Queensland, Brisbane, Queensland 4072, Australia

Supporting Information

ABSTRACT: Surfactant-free CuAgSe nanoparticles were successfully synthesized on a large scale within a short reaction time via a simple environmentally friendly aqueous approach under room temperature. The nanopowders obtained were consolidated into pellets for investigation of their thermoelectric properties between 3 and 623 K. The pellets show strong metallic characteristics below 60 K and turn into an *n*-type semiconductor with increasing temperature, accompanied by changes in the crystal structure (i.e., from the pure tetragonal phase into a mixture of tetragonal and orthorhombic phases), the electrical conductivity, the Seebeck coefficient, and the thermal conductivity, which leads to a figure of merit (ZT) of 0.42 at 323 K. The pellets show further interesting temperature-dependent transition from *n*-type into *p*-type in electrical conductivity arising from phase transition (i.e., from the mixture phases into cubic phase), evidenced by the change of the Seebeck coefficient from −28 μV/K into 226 μV/K at 467 K. The ZT value increased with increasing temperature after the phase transition and reached 0.9 at 623 K. The sintered CuAgSe pellets also display excellent stability, and there is no obvious change observed after 5 cycles of consecutive measurements. Our results demonstrate the potential of CuAgSe to simultaneously serve (at different temperatures) as both an *n*-type and a *p*-type thermoelectric material.

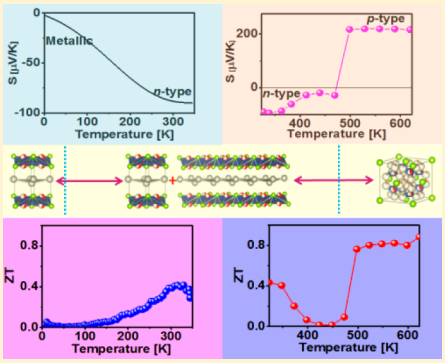

1. INTRODUCTION

Direct conversion of heat into electricity on the basis of the Seebeck effect (i.e., thermoelectric technology, TE) shows great potential in harvesting waste heat, because it is environmentally friendly, stable, reliable, and applicable in remote areas.[1−4] This technology could lead to significant savings on energy consumption and reduce carbon emissions. It remains a challenge, however, for wide practical applications because of its low conversion efficiency arising from the lack of environmentally friendly, high performance, and low cost thermoelectric materials. The thermoelectric performance of materials is characterized by the "figure of merit" (ZT), which is described by eq 1.

$$ZT = \frac{S^2\sigma}{\kappa}T \quad (1)$$

in which S is the Seebeck coefficient, σ is the electrical conductivity, κ is the thermal conductivity, and $S^2\sigma$ is defined as the power factor, while T is the measurement temperature.[5−11]

Great efforts have been devoted to optimization of these 3 factors for achieving a high ZT. It is very challenging, however, to simultaneously optimize them; an alternative way is the introduction of nanostructures or the use of phonon-glass electron-crystal (PGEC) or phonon-liquid electron-crystal (PLEC) materials to reduce the thermal conductivity (while the power factor is not seriously degraded) to achieve a high ZT.[1−8,12,13] For example, the ZT value of *p*-type PbTe can be improved to over 2 by the introduction of nanoprecipitates through chemical doping.[14] The concept of PGEC was proposed by Slack et al. in 1979, and it has attracted considerable attention in the regime of thermoelectric materials. On the basis of PGEC, a similar concept PLEC was proposed in 2012 during investigation of thermoelectric properties of nonstoichiometric superionic copper selenide ($Cu_{2-x}Se$), which exhibits a ZT of 1.6 at 1000 K due to the phase change from rigid crystal to disordered PLEC state, which was composed by highly disordered cuprous cations around with the chalcogen sublattice. The copper ions behave like a liquid at high temperature and minimize the thermal

Received: October 10, 2014
Published: November 24, 2014

   dx.doi.org/10.1021/ja510433j | J. Am. Chem. Soc. 2014, 136, 17626−17633

conductivity.[12] Another good example of PLEC material is nonstoichiometric copper sulfide $Cu_{1.97}S$, which has the maximum ZT of 1.7 at 1000 K accompanied by an obvious phase transition from low chalcocite phase to PLEC state at around 400 K.[15] Besides copper chalcogenides, silver chalcogenides experienced similar phase transition and anomalous TE performance was also observed.[16] Although the phase transition related transports are common in PLEC materials, its mechanism was rarely studied.[12,15−17]

The high ZT of the PLEC has motivated substantial efforts in searching for high performance thermoelectric materials with a similar superionic structure. As an important ternary selenide, CuAgSe is such a candidate with the superionic property due to the mobility of both Cu^+ and Ag^+ ions at high temperature. Extremely high electron mobility at low temperature and a ZT of 0.15 at room temperature and a ZT of 0.95 at 623 K have been reported in bulk CuAgSe.[18,19]

It should be noted that most research has been focused on bulk CuAgSe prepared by the solid state reaction at high temperature (>1000 K),[18,19] and there is no report on the thermoelectric properties of CuAgSe sintered from its nanostructures due to the difficulties in efficient preparation of CuAgSe nanomaterials on a large scale. Small-scale CuAgSe nanotubes and dendrites can be prepared from Se and Ag_2Se nanotemplates, respectively.[20,21] Herein, we synthesize surfactant-free CuAgSe nanoparticles from $Cu(NO_3)_2$, $AgNO_3$, and Se precursors via a robust ambient approach (Scheme 1). The

Scheme 1. Schematic Illustration of Synthesis Process

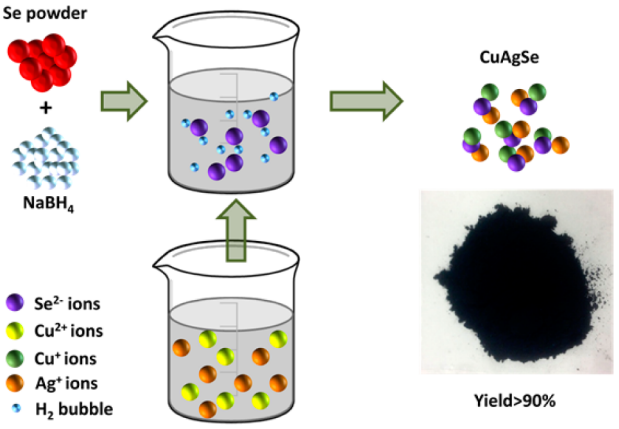

whole synthesis process is very simple and effective (within 30 min) with a high yield (over 90%). More importantly, the whole reaction is in an aqueous system without heating or any expensive/toxic solvents, and dangerous waste. This simple and scalable method is capable of producing large amounts of surfactant-free CuAgSe nanoparticles for investigation of the thermoelectric properties of their sintered pellets between 3 and 623 K. The results show their excellent electric conductivity at low temperature (below 60 K) and semiconducting characteristics at high temperature, which can be reversibly switched from metallic conductor, n-type semiconductor to p-type semiconductor by varying the temperature. The ZT values of CuAgSe made from nanoparticles are 0.42 at 323 K and 0.9 at 623 K, respectively.

2. EXPERIMENTAL SECTION

2.1. Synthesis of CuAgSe Nanoparticles. All chemicals were bought from Sigma-Aldrich Pty. Ltd. and used as received without any further purification. In a typical synthesis, 3.16 g (40 mmol) of Se powder (100 mesh, ≥99.5%) and 4.54 g (120 mmol) of $NaBH_4$ (caplets, ≥98%) were dispersed in 400 mL of distilled water, and the mixture was stirred for 25 min under the protection of Ar at room temperature to form a colorless selenium precursor solution. 9.7 g (40 mmol) of $Cu(NO_3)_2{\cdot}3H_2O$ (97%) and 6.8 g (40 mmol) of $AgNO_3$ (97%) were completely dissolved in 400 mL of distilled water, and then quickly added into the Se-precursor solution to generate black precipitates. The black product was washed with distilled water several times, and then dried to a constant weight at 80 °C in a vacuum to give a yield over 90%.

2.2. Characterization. X-ray diffraction (XRD) studies were carried out at room temperature with an X-ray diffractometer (GBC-MMA) using Cu Kα radiation (λ = 0.154 nm). The low-temperature XRD in the range of 20 and 300 K were performed using a PANalytical diffractometer with Cu Kα radiation (λ = 0.154 nm). Scanning electron microscopy (SEM) was conducted on a JEOL JSM-7500FA microscope. Transmission electron microscopy (TEM) was performed using a JEOL JEM-2011 microscope with an accelerating voltage of 200 kV. X-ray photoelectron spectroscopy (XPS) was conducted using a SPECS PHOIBOS 100 Analyzer installed in a high-vacuum chamber with the base pressure below 10^{-8} mbar. X-ray excitation was provided by Al Kα radiation with the photon energy $h\upsilon$ = 1486.6 eV at the high voltage of 12 kV and power of 120 W. The binding energy spectra were recorded at the pass energy of 20 eV in the fixed analyzer transmission mode. All the spectra were calibrated with C 1s at 284.6 eV. Analysis of the XPS data was carried out using the commercial Casa XPS 2.3.15 software package.

2.3. Thermoelectric Properties Test. The as-synthesized CuAgSe nanoparticles (3 g) were loaded into a graphite die with a diameter of 20 mm and sintered into a pellet at 430 °C under 65 MPa pressure for 10 min by the spark plasma sintering (SPS) technique. The pellet was cut into rectangular pieces with dimensions of 4 × 13 × 1.2 mm^3 for thermoelectric characterization.

Low-temperature thermoelectric performance (i.e., from 3 to 350 K) was tested on a physical properties measurement system (PPMS). The Seebeck coefficient, electrical conductivity, and thermal conductivity, as well as the ZT values, were obtained simultaneously. The high-temperature Seebeck coefficient and electrical conductivity were measured from 323 to 623 K under helium atmosphere using an Ozawa RZ2001i (Japan) instrument. A Linseis LFA1000 (Germany) was used to determine the thermal diffusivity of samples, which were cut and polished into Ø10 × 1 mm^2 disks. The thermal conductivity (κ) was calculated using the equation $\kappa = D \times C_p \times \rho$, where D is the thermal diffusivity, C_p is the heat capacity, and ρ is the mass density of the specimen, determined by the Archimedes method. The temperature dependence of the heat capacity (C_p) was determined using the differential scanning calorimeter (DSC) method on a DSCQ100 instrument with a heating rate of 10 K/min and a N_2 flow of 50 mL/min.

2.4. Theoretical Calculations. The calculations of band structures of tetragonal and cubic α-phase CuAgSe were performed using the generalized gradient approximation[22] treated by the Perdew−Burke−Ernzerh (PBE) of exchange-correlation potential, as implemented in the DMol3 module in Materials Studio.[23,24] An all electrons double numerical atomic orbital augmented by d-polarization functions (DNP) was used as basis set, which has been successfully used to determine the electronic structures of nanomaterials.[25] The calculation models were built according to the experimental lattice parameters.[26,27] The electronic Brillouin zone was sampled by using a Monkhorst−Pack grid of sample spacing 0.002 $Å^{-1}$.

3. RESULTS AND DISCUSSION

It is well-known that CuAgSe has tetragonal, orthorhombic, and cubic structures (Figure 1), in which the tetragonal structure has lattice parameters a = 4.1 Å, b = 4.05 Å, and c = 6.31 Å, and the orthorhombic one is an essentially a pseudotetragonal structure with a large supercell (a = 4.1 Å, b = 20.35 Å, and c = 6.31 Å).[26,28] The "tetragonal structure" here is not strictly

dx.doi.org/10.1021/ja510433j | J. Am. Chem. Soc. 2014, 136, 17626−17633

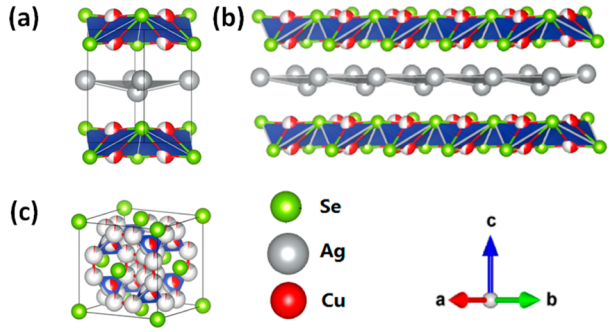

Figure 1. Schematic crystal structures of CuAgSe: (a) low temperature tetragonal CuAgSe; (b) low temperature orthorhombic CuAgSe; (c) high temperature cubic CuAgSe. The mixed gray and red mean randomly occupied by Ag or Cu atoms.

tetragonal as $a \neq b$ (a = 4.1 Å and b = 4.05 Å). There is no big difference between these two structures, except that the orthorhombic structure features a sequence that repeats itself periodically every five tetragonal cells in the b direction. They both possess a similar layered structure consisting of alternating stacking of the Ag and CuSe layers, in which Ag atoms almost lie in the same plane and are bonded closely to Se atoms, allowing high mobility of Ag atoms and the formation of Ag−Ag metallic bonds.[26] Se atoms form a squashed tetrahedron, in which each corner is shared with adjacent tetrahedron, and Cu atoms are offset from the center within the tetrahedron. Each tetragonal cell contains two CuAgSe molecules, and the orthorhombic one has 10 molecules. Both the tetragonal and the orthorhombic structures are stable at low temperature and can be reversibly transformed into the cubic structure at high temperature.

The crystal structure of the as-synthesized CuAgSe nanoparticles was determined by X-ray diffraction, and their XRD pattern is compared with those of standard orthorhombic CuAgSe (JCPDS 10−0451, black vertical lines) and tetragonal CuAgSe (JCPDS 25−1180, red vertical lines) in Figure 2(a). Most peaks and their intensity ratios are well matched with those of the orthorhombic structure, except for the peaks at 2θ = 43.16° (0,0,3), 44.02° (2,0,0), and 44.5° (0,2,0), which are

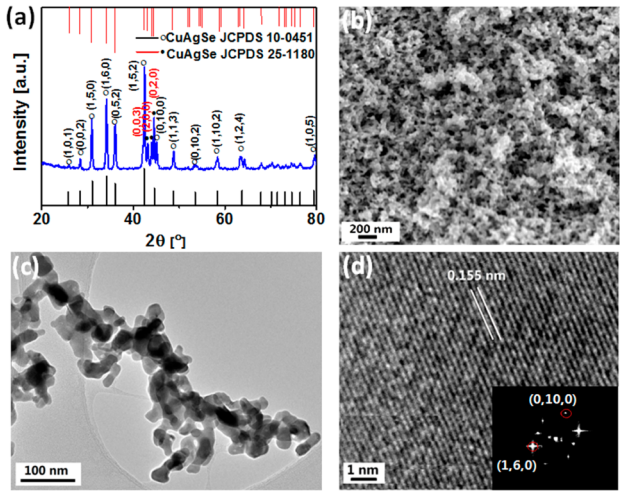

Figure 2. (a) X-ray diffraction pattern, (b−d) SEM, TEM, and HRTEM images of as-synthesized CuAgSe nanoparticles; inset picture in (d) is Fast Fourier Transform pattern from HRTEM image.

marked with black dots in Figure 2(a) and can be solely attributed to the tetragonal structure. The mixture of tetragonal and orthorhombic structures is attributed to the minor difference between them, and this could be caused by the nanoscale effects and the distortion of the crystal during the formation of nanoparticles.

The SEM and TEM images in Figure 2(b,c) show irregular CuAgSe nanoparticles with an average diameter of 20 nm. The high resolution TEM (HRTEM) image in Figure 2(d) clearly shows an interplanar spacing of 0.155 nm, which is consistent with the (1,10,2) plane. The fast Fourier transform (FFT) image in the inset of Figure 2(d) shows the diffraction spots from the (0,10,0) and (1,6,0) crystal planes.

The resultant CuAgSe nanoparticles were further characterized by XPS, and Figure 3 shows the binding energies of

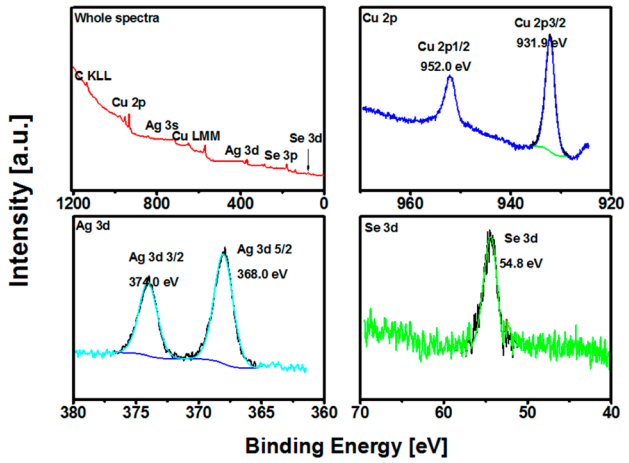

Figure 3. XPS spectra of the CuAgSe nanopowder.

elements in the sample after calibration with the binding energy of C 1s at 284.6 eV. The absence of other elements apart from C, O, Cu, Ag, and Se indicates the high purity of the nanoparticles. The two distinct peaks at 931.9 and 952.0 eV in the Cu 2p spectrum are assigned to Cu 2p3/2 and Cu 2p1/2 of Cu^+, respectively. The absence of a satellite peak at ∼942.47 eV further supports the identification of the copper element as Cu^+, rather than Cu^{2+}.[29] The peaks located at 368.0 and 374.0 eV represent the 3d5/2 and 3d3/2 orbital of Ag^+, respectively. The Se 3d5/2 peak from Se^{2-} is located at 54.8 eV.[11,30] The binding energies of Cu^+, Ag^+, and Se^{2-} ions are consistent with previous reports, demonstrating the formation of pure CuAgSe nanoparticles.[20,31−33]

The above results demonstrate that pure CuAgSe nanoparticles can be simply synthesized from $Cu(NO_3)_2$, $AgNO_3$, and Se precursors in aqueous solution. The formation mechanism is not as simple as Scheme 1 shown, however, and includes the following key steps. First, selenium powder is reduced by $NaBH_4$ to form the colorless Se-precursor solution, as shown in reaction 2.

$$2Se + 4NaBH_4 + 7H_2O \rightarrow 2NaHSe + Na_2B_4O_7 + 14H_2\uparrow \quad (2)$$

After addition of a mixture of $Cu(NO_3)_2$ and $AgNO_3$ into the Se-precursor solution, the excess $NaBH_4$ in situ reduces Cu^{2+} into Cu^+ through reaction 3 because the standard reduction potential of Cu^{2+}/Cu^+ (0.153 V) is much smaller than that of Ag^+/Ag (0.8 V).

dx.doi.org/10.1021/ja510433j | J. Am. Chem. Soc. 2014, 136, 17626−17633

$$2NaBH_4 + 2Cu^{2+} + 4H_2O \rightarrow 2Cu^{+} + 2H^{+} + 7H_2 \uparrow + 2NaBO_2 \quad (3)$$

Then, $AgNO_3$ reacts with NaHSe to form Ag_2Se precipitate first, due to the lower solubility of Ag_2Se compared to Cu_2Se [$K_{sp}(Ag_2Se) = 2 \times 10^{-63.7}$; $K_{sp}(Cu_2Se) = 1.58 \times 10^{-60.8}$], followed by the reaction of fresh Ag_2Se with Cu_2Se to form alloyed CuAgSe nanoparticles through reaction 4.[20,21]

$$Ag_2Se + Cu_2Se \rightarrow 2CuAgSe \quad (4)$$

To prove the above mechanism, a control experiment was conducted by using less reducing agent (i.e., Se/$NaBH_4$ molar ratio of 1:2) and using CuCl to replace $Cu(NO_3)_2$. After the Se powder was completely reduced by $NaBH_4$ to form a clear solution, the $AgNO_3$ solution was added into the Se-precursor solution to form a black suspension. A portion of the suspension was separated from solution and purified for analysis. CuCl powder was dissolved in HCl solution and added into black suspension under stirring. The mixture was stirred for 30 min at room temperature, and then the precipitate was collected. The XRD patterns and morphology of the black precipitates collected before and after addition of CuCl solution are shown in Figure S1 in the Supporting Information. The results demonstrate that the precipitate collected before the addition of CuCl is pure Ag_2Se (JCPDS 24−1041), and the one collected after addition of CuCl is CuAgSe mixed with a small amount of Ag_2Se. These results demonstrate that residual Se^{2-} ions react with Cu^{+} to form Cu_2Se, which further reacts with Ag_2Se to form CuAgSe. This mechanism is further supported by the reaction between the as-prepared Cu_2Se nanoparticles and the Ag_2Se nanoparticles. As displayed in Figure S2, the typical diffraction peak (1,6,0) from orthorhombic CuAgSe was observed in the mixture after it was stirred for 10 min at room temperature. The intensity of this peak was increased in the mixture after 30 h aging time under stirring, indicating the increased amount of CuAgSe nanoparticles in the mixture, although the Cu_2Se and Ag_2Se nanoparticles were not completely transformed into CuAgSe.

According to the reaction mechanism, the compositions of the final products strongly depend on the precursor ratio of Cu^{2+}:Ag^{+}:Se^{2-} (R, molar ratio) and the amount of $NaBH_4$. As shown in Figure S3(a), CuAgSe nanoparticles can only be obtained with a ratio of 1:1:1. When a ratio of 1:2:2 was used, the product is a mixture of CuAgSe, Ag_2Se (JCPDS 24−1041), and Ag (JCPDS 65−2871) nanoparticles, as indicated by the XRD pattern. In the case of 2:2:1 ratio, the product is a mixture of Ag_2Se and Ag nanoparticles. The appearance of Ag in both cases could be due to the reduction of Ag^{+} by slightly excess $NaBH_4$. When a 2:1:2 ratio was adopted, the product contained CuAgSe and a small amount of Cu_2Se (JCPDS 65−2982).

The role of $NaBH_4$ is to reduce both the Se powder and the $Cu(NO_3)_2$, and it is crucial to control the amount of $NaBH_4$. The ideal amount of $NaBH_4$ should be 3 times that of $Cu(NO_3)_2$ (or $AgNO_3$ or Se), i.e., their molar ratio r should be 3:1. When an inadequate amount of $NaBH_4$ was used (i.e., r = 2:1), the product is a mixture of Ag_2Se, CuSe, and Se, as shown in Figure S3(b), because $NaBH_4$ is not enough for reduction of the Se powder and $Cu(NO_3)_2$. When excessive $NaBH_4$ (e.g., r = 4:1 or 8:1) was used, Ag and Cu_2O were observed in the products [Figure S3(b)]. The formation of Cu_2O could be due to the increased solution pH caused by the hydrolysis of $NaBH_4$ and sodium borate.

This simple green method is capable of producing CuAgSe nanoparticles on the gram scale in a one-pot reaction. The resultant surfactant-free nanoparticles can be directly used without surface modification for fabrication of pellets for thermoelectric study. Figure 4(a) presents a SEM image of the

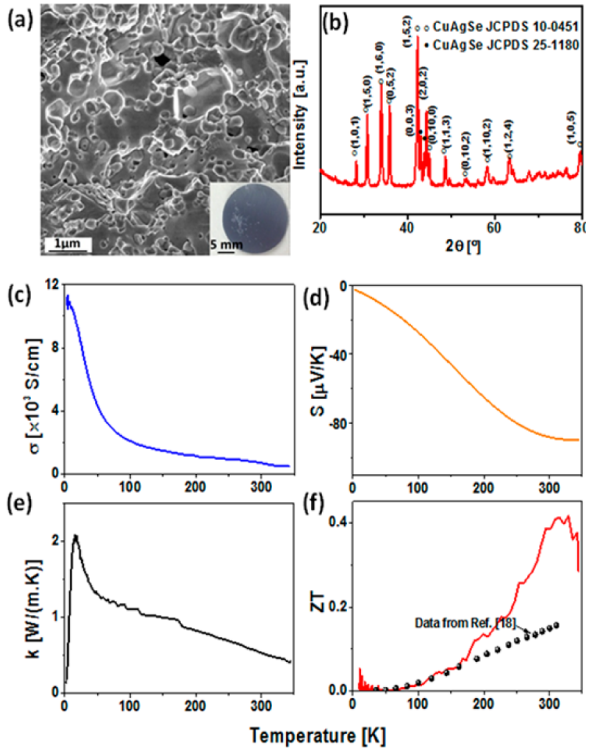

Figure 4. (a) SEM image of the consolidated pellet from the prepared CuAgSe nanoparticles, inset is the coin-like pellet; (b) XRD pattern of the pellet; (c−f) TE performance of the sintered CuAgSe nanoparticles from 3 K to room temperature.

cross-section of a pellet [the inset in Figure 4(a)], which was made from as-synthesized CuAgSe nanoparticles that were consolidated at 430 °C for 10 min under 65 MPa using the SPS technique. The relative density is about 90%, and the SEM image shows nanoscale pores and particles in the pellet, although most nanoparticles were coarsened and aggregated to form larger grains. Compared with nonsintered powder, there is no distinct difference in its room-temperature crystal structure [Figure 4(b)], except that the diffraction intensity of the crystal planes [e.g., (0,0,3) peak] of the tetragonal phase is improved.

The pellet was cut into pieces for thermoelectric investigation, and Figure 4(c−f) presents the results obtained on a PPMS instrument from low temperature to room temperature. The temperature dependence of the electrical conductivity in Figure 4(c) clearly demonstrates the metallic behavior of the pellet below 60 K, as indicated by the gradual increase of the electrical conductivity from 800 S/cm at room temperature to 3500 S/cm at 60 K, followed by a rapid increase to 11330 S/cm at 3 K. The tendency of the Seebeck coefficient is opposite to that of the electrical conductivity, and it decreases from −90 μV/K to nearly 0 with temperature decreasing from room temperature to 3 K [Figure 4(d)].

The variation of the thermal conductivity with temperature is shown in Figure 4(e). It rises with temperature decreasing to reach the maximum value of 2.1 W/(m·K) at 22 K, and then decreases to 0.2 W/(m.K) at 3 K. The ultralow thermal

dx.doi.org/10.1021/ja510433j | J. Am. Chem. Soc. 2014, 136, 17626−17633

conductivity [0.5 W/(m·K)] at room temperature can be attributed to the large lattice anharmonicity caused by the structure, which is reminiscent of amorphous solids.[18] In addition, the nanoscale particles, pores, and grain boundaries that are present in the pellet also make contributions to the low thermal conductivity, because they can effectively scatter different wavelengths of phonons. The *ZT* value of the pellet is displayed in Figure 4(f), and it gradually increases with increasing temperature to achieve a value of 0.42 at 323 K, and then decreases with temperature. Compared with bulk CuAgSe[18] [black dotted line in Figure 4(f)], the pellet made from nanoparticles exhibits a higher *ZT* due to extremely low thermal conductivity.

To investigate the abrupt metallic-*n* transition at around 60 K, temperature-dependent XRD of pellet was performed in the range of 20 to 300 K (Figure 5). As labeled by black and red

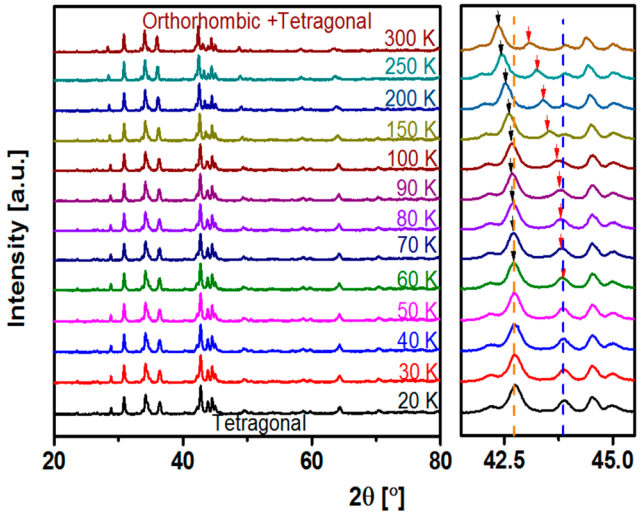

Figure 5. Temperature dependent XRD patterns for the sintered CuAgSe pellet from 20 to 300 K.

arrows in Figure 5, with the temperature decreasing from 300 to 60 K, the strongest peak $(1,5,2)_{orth}$ shifted to right. Meanwhile, the two peaks of $(0,0,3)_{tetra}$ and $(2,0,0)_{tetra}$ gradually merged into one at around 70–60 K. The sample remained the same crystal structure below 60 K. The dependence of lattice parameters on temperature was calculated and shown in Table S1. Apparently, both the lattice parameters and the volume of unit cell reduced with decrease of temperature.

The shrinkage of unit volume with temperature dropping is understandable. As illustrated previously, the tetragonal and orthorhombic CuAgSe are almost the same except that the later one has a sequence which repeats itself periodically every five tetragonal cells in the *b* direction. The relative positions of atoms could be rearranged with decrease of temperature, leading to the structure transition from orthorhombic to tetragonal phase. This phase transition makes the structure more symmetric because the unit cell changes from bigger orthorhombic cell to smaller tetragonal one, which benefits to the reduction of scatterings of phonons and electrons. The gradually reduced electron scattering led to a high mobility, while reduced phonon scattering led to the increase in thermal conductivity with temperature decreasing to 22 K [Figure 4(e)].

The low temperature transport properties of CuAgSe were characterized by Hall Effect measurements. Detailed device assembly, the measured relationship between the Hall resistivity and the magnetic field, the calculated carrier density (*n*), and the carrier mobility (μ) are presented in Figure 6(a–d). The

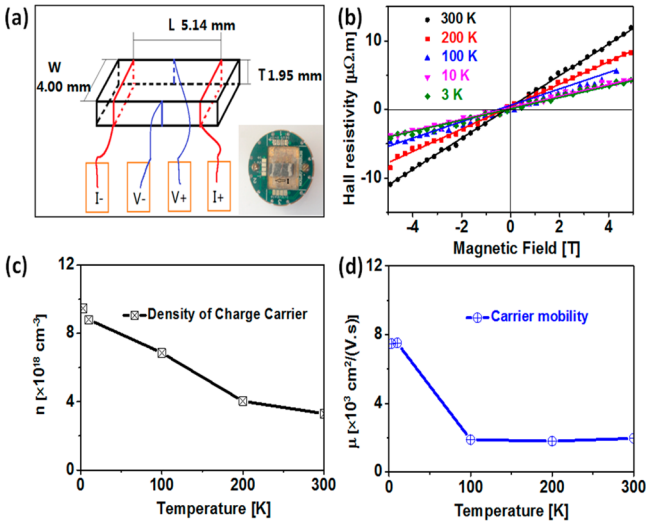

Figure 6. (a) Sample connections and dimensions for the measurement of Hall effect, inset is the assembled device for testing; (b) Hall resistivity as a function of magnetic field; (c) calculated *n* and (d) calculated μ as functions of temperature.

detailed calculations and results are presented in the Supporting Information (Section 3 and Table S2). The results show that electrons are the main charge carriers in CuAgSe below 300 K. The carrier density (*n*) is approximately 10^{18} and decreases with rising temperature, while the carrier mobility first decreases from 7478 to 1798 $cm^2/(V·s)$ with temperature increasing from 3 to 200 K, then slightly increases to 1966 $cm^2/(V·s)$ at 300 K. The carrier density is almost the same but the carrier mobility is significantly reduced by nanostructure compared with bulk CuAgSe.[18,19]

The thermoelectric properties of sintered CuAgSe nanoparticles above room temperature were further investigated, and Figure 7 displays the results measured from room temperature to 623 K. The differences between the results around room temperature shown in Figures 4 and 7 originated from the error of different instruments. A reversible first order phase transition is proved by the heating–cooling DSC curves displayed in Figure S4(a). This means the occurrence of a reversible phase transition during the heating process (i.e., changing from orthorhombic CuAgSe into cubic CuAgSe), which has been demonstrated in previous reports.[27,28] Like other Cu and Ag based PLEC materials with phase transition,[16,17] the temperature dependences of the electrical conductivity, Seebeck coefficient, thermal conductivity, and specific heat of CuAgSe show an interesting transition accompanied by its phase transition. As presented in Figure 1(c), the high-temperature cubic phase is composed of a face-centered-cubic Se lattice with Ag/Cu cations that are randomly distributed among the tetrahedral sites. This unique structure ensures the high mobility of the Ag/Cu cations and leads to superionic property. The electrical conductivity of CuAgSe [Figure 7(a)] decreases from 1040 to 400 S/cm with increasing temperature from 323 to 467 K. After the phase transition, the scattering of charge carriers is dramatically increased by the highly disordered Ag^+ and Cu^+ ions, resulting in a further decrease in the electrical conductivity to 100 S/cm, which

dx.doi.org/10.1021/ja510433j | J. Am. Chem. Soc. 2014, 136, 17626–17633

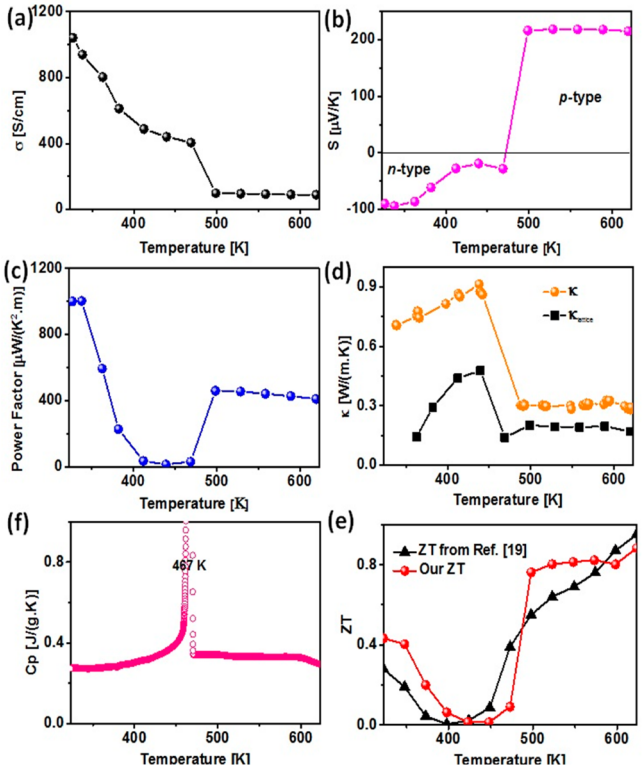

Figure 7. TE performance of sintered CuAgSe nanoparticles from 323 to 623 K: (a) electrical conductivity; (b) Seebeck coefficient; (c) power factor; (d) thermal conductivity; (e) specific heat capacity; (f) *ZT* value.

remains unchanged up to 623 K. The independence of the electrical conductivity from temperature is related with the band structure of *p*-type CuAgSe, which is shown in Figure 8 and discussed late.

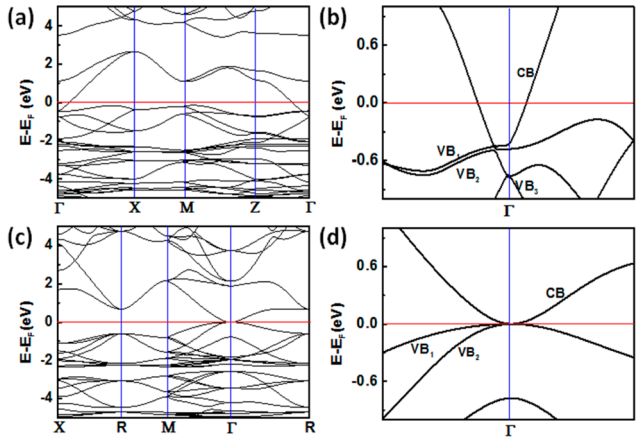

Figure 8. Calculated band structure for (a) tetragonal CuAgSe; (b) *α*-phase cubic CuAgSe; and (c,d) magnified part of Γ point.

The negative value of the Seebeck coefficient [Figure 7(b)] demonstrates that orthorhombic CuAgSe is an intrinsic *n*-type semiconductor before the phase transition. The Seebeck coefficient decreases from −90 μV/K to around −20 μV/K with increasing temperature from room temperature to the phase transition temperature. A sudden *n*−*p* transition occurs with the phase transition and the cubic CuAgSe exhibits a nearly constant positive Seebeck coefficient of 226 μV/K [Figure 7(b)]. The transition of Seebeck coefficient (or type of charge carrier) is essentially due to the change of band structure, which is associated with the change of crystal structure arising from the variation of temperature. Increase of temperature leads to the transition from mixed orthorhombic and tetragonal phases into cubic structure, which has been reported in the bulk CuAgSe.[19]

The overall and lattice thermal conductivities ($\kappa_{lattice} = \kappa\text{-}L\sigma T$, $L = 2.1 \times 10^{-8}$ (W·Ω)/K^2), Wiedemann−Franz Law) of CuAgSe in the range of 323 to 623 K are presented in Figure 7(d). The overall thermal conductivity increases from 0.75 W/(m·K) at 370 K to around 0.92 W/(m·K) at 445 K, accompanied by increasing lattice thermal conductivity ($\kappa_{lattice}$) from 0.15 W/(m·K) at 370 K to 0.5 W/(m·K) at 445 K. After the phase transition, the overall thermal conductivity is reduced to around 0.3 W/(m·K), owing to the high mobility of Cu^+ and Ag^+ cations. The lattice thermal conductivity slightly increases to 0.2 W/(m·K), as the contribution of charge carriers is inhibited by the low electrical conductivity. The low thermal conductivity of pellet made from nanoparticles is further addressed by comparing with that of pellet sintered from bulk counterpart (Figure S5). Bulk CuAgSe was prepared by annealing CuAgSe nanoparticles at 600 °C for 24 h in a sealed quartz tube under vacuum, which was ground into powder [Figure S5(a)] and sintered by SPS at 430 °C for 10 min under 60 MPa. The cross section shows high density and absence of nanostructures in the pellet [Figure S5(b)]. The X-ray diffraction pattern is same to that of original CuAgSe nanopowder [Figure S5(c)]. The thermal conductivity of the pellet sintered from annealed CuAgSe is higher than that of pellet from nanopowder, which supports the presence of nanostructures can effectively decrease the thermal conductivity.

The temperature-dependent *ZT* of our CuAgSe nanoparticles is also compared with literature values from bulk CuAgSe[19] in Figure 7(f). A similar temperature dependence is observed in both nanostructured and bulk CuAgSe,[19] although our room-temperature *ZT* is higher than previous reports (i.e., 0.42 vs 0.15 at 323 K from PPMS; 0.42 vs 0.28 at 323 K from high-temperature instruments). In the range of 500−575 K, our *ZT* values (∼0.8) are also higher than the literature values.[19] Our *ZT* values above 575 K are comparable to the bulk value (0.9 vs 0.95 at 623 K) due to the extremely low thermal conductivity. The valley-like *ZT* profiles suggest the minimum value near the phase transition temperature (467 K), and it drastically increased from 0.1 at 470 K to 0.8 at 500 K. This anomalous behavior is consistent with previous reports on thermoelectric materials with phase transition.[16,17]

To further understand the *n*−*p* transition of electrical conductivity, the electronic structures of tetragonal and cubic CuAgSe were calculated. Figure 8(a) illustrates the calculated band structure of tetragonal CuAgSe at the PBE level. Figure 8(b) is the magnified band structure at Γ point near the Fermi level. They both clearly show that one of conduction bands is crossing the Fermi level along the *Z*−Γ and Γ−*X* lines, while the top of valence band is just located below the Fermi level.[18] Thus, the tetragonal CuAgSe should possess two kinds of charge carriers. The main charge carriers are electrons, however, and the conductivity is *n*-type. In addition, the conduction bands are relative sparse than valence bands, and more electrons are located near Fermi level as shown by Figure 8(a) and its density of states (DOS) [Figure S6(a)]. Figure

dx.doi.org/10.1021/ja510433j | J. Am. Chem. Soc. 2014, 136, 17626−17633

8(b) also demonstrates that both the conduction bands and valence bands are highly asymmetric at the Γ point, which means the tetragonal structure is highly anhomonic or disordered, leading to low thermal conductivity. Figure 8(c) is the calculated band structure of cubic CuAgSe and Figure 8(d) is the magnified band structure at Γ point where no band gap was observed.

The Seebeck coefficient could be expressed by the following eq 5:

$$S = A \times T \times \frac{m^*}{n^{2/3}} \tag{5}$$

in which A is a constant, T is temperature, n is the charge carrier density, m^* is the effective mass of charge carriers and equal to the reciprocal of the curvature of band edge when the band gap is 0 eV at Γ point. As displayed in Figure 8(d), the curvature of conduction band edge (CB) is bigger than any of the valence band edge (VB_1 and VB_2), the effective mass of holes ($m_h^* = m_{VB_1}^* + m_{VB_2}^*$) is heavier than the absolute value of electrons ($|m_e^*|$). The whole effective mass is positive, e.g., $m^* = m_e^* + m_h^* > 0$, which results in a positive S [Figure 7(b)]. In addition, the high-temperature phase CuAgSe possesses a cubic-face-centered Se frame, but both the conduction band and valence band at Γ point show high asymmetry [Figure 8(d)]. This implies the cations sublattice (Cu^+ and Ag^+) is highly disordered, which can enhance the phonon scatterings and reduce the thermal conductivity. Although the DOS of cubic structure shows the same concentration near Fermi level [Figure S6(b)] as tetragonal phase, the electrical conductivity is still low due to the disordered cations. It has known that the electrical conductivity (σ) of an intrinsic semiconductor can be expressed by eq 6,[16] in which $f(T)$ is a function almost independent with temperature (T), E_g is the band gap, k_B is Boltzmann constant. Because of that the band gap of p-type CuAgSe is 0 eV [Figure 8(d)], the electrical conductivity is almost a constant with temperature increasing.

$$\sigma = f(T) \times \exp\left(-\frac{E_g}{k_B T}\right) \tag{6}$$

From the perspective of practical application, the cycling stability of thermoelectric materials is a very important parameter during long-term operation. Therefore, we tested the stability of the consolidated CuAgSe pellet in a sealed chamber (Ozawa 200li) filled with a low pressure helium, and measured its electrical conductivity and Seebeck coefficient through 5 cycles of heating and cooling from room temperature to 623 K. There are no big differences in the morphology, composition, and appearance of the pellet before and after 5 cycles. The morphology, composition, electrical conductivity, and Seebeck coefficient are plotted in Figure 9(a–d). Good reproducibility is observed in these data obtained from different cycles. The heating–cooling cycles demonstrate the good stability of the pellet, which is also supported by the zero loss in weight during the thermogravimetric analysis (TGA) [Figure S4(b)]. No oxidation or evaporation occurred during analysis. In addition, XPS was also employed to characterize the sample after 5 cycles (Figure S7). No other elements were detected, and the valence states of Cu, Se and Ag did not change. These results demonstrate that our CuAgSe pellet consolidated from nanoparticles is stable under cycling test.

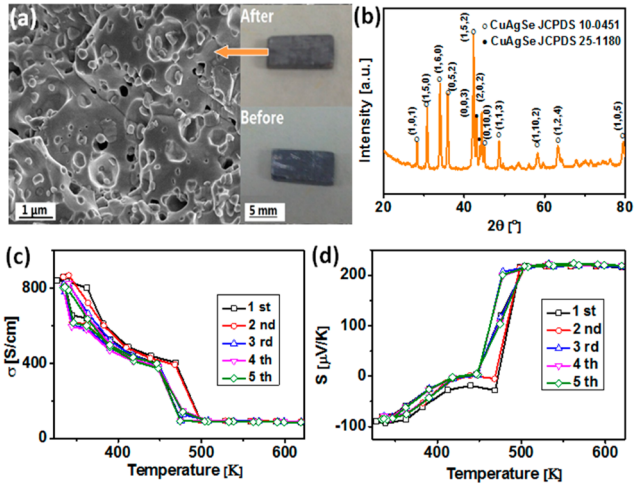

Figure 9. TE properties of sintered CuAgSe nanoparticles tested over 5 cycles (heating and cooling): (a) SEM image of pellet after 5 cycles; right side is the pellet before and after 5 cycles; (b) XRD pattern after 5 cycles; (c) electrical conductivity; (d) Seebeck coefficient.

4. CONCLUSION

Large-scale surfactant-free CuAgSe nanoparticles were successfully synthesized via a robust environmentally friendly aqueous method. The resultant CuAgSe nanoparticles were sintered into pellets by an advanced SPS technique for thermoelectric investigation in the range of 3 to 623 K. The results show an interesting temperature-dependent transport property accompanied by a phase transition; i.e., sintered CuAgSe nanoparticles exhibit metallic characteristics below 60 K, n-type semiconductor behavior in the range of 60 to 480 K, and p-type semiconductor behavior above 480 K. The pellet displays a ZT of 0.42 at 323 K and 0.9 at 623 K, and exhibits excellent cycling stability. The temperature-dependent n–p transition and the excellent stability of CuAgSe enable it to simultaneously serve as an n-type and p-type (at different temperatures) thermoelectric candidate for conversion of heat into electricity.

■ ASSOCIATED CONTENT

Ⓢ Supporting Information

Results of control experiment, including XRD patterns and SEM images, and DSC, TGA, DOS and XPS curves of the CuAgSe pellet, calculated lattice parameters and transport properties, as well as the Hall Effect calculations. This material is available free of charge via the Internet at http://pubs.acs.org.

■ AUTHOR INFORMATION

Corresponding Author

zhenl@uow.edu.au

Notes

The authors declare no competing financial interest.

■ ACKNOWLEDGMENTS

C. Han gratefully acknowledges the Chinese Scholarship Council (CSC) for his scholarship. Z. Li and M. Lu acknowledge support from the Australian Research Council (ARC) through the Discovery Projects DP130102699 and DP130102274. S. Dou is grateful for support from the Baosteel-Australia Research Centre (BARC) through the project BA110011 and from the ARC through the Linkage Project LP120200289. The authors would like to thank Dr. Tania Silver

for polishing the manuscript, and ISEM and the Electronic Microscope Centre (EMC) for their support.

REFERENCES

(1) Bell, E. *Science* **2008**, *321*, 1457.
(2) Xiao, C.; Xu, J.; Li, K.; Fen, J.; Yang, J. L.; Xie, Y. *J. Am. Chem. Soc.* **2012**, *134*, 4287.
(3) Kraemer, D.; Poudel, B.; Feng, H. P.; Caylor, J. C.; Bo, Y.; Yan, X.; Ma, Y.; Wang, X. W.; Wang, D. Z.; Muto, A.; McEnaney, K.; Chiesa, M.; Ren, Z. F.; Chen, G. *Nat. Mater.* **2011**, *10*, 532.
(4) Liu, W. S.; Zhang, Q. Y.; Lan, Y. C.; Chen, S.; Yan, X.; Zhang, Q.; Wang, H.; Wang, D. Z.; Chen, G.; Ren, Z. F. *Adv. Energy Mater.* **2011**, *1*, 577.
(5) Hoshino, A.; Fujioka, K.; Oku, T.; Nakamura, S.; Suga, M.; Yamaguchi, Y.; Suzuki, K.; Yasuhara, M.; Yamamoto, K. *Immunology* **2004**, *48*, 985.
(6) Pichanusakorn, P.; Bandaru, P. *Mater. Sci. Eng., R* **2010**, *67*, 19.
(7) Shakouri, A. *Annu. Rev. Mater. Res.* **2011**, *41*, 399.
(8) Snyder, G. J.; Toberer, E. S. *Nat. Mater.* **2008**, *7*, 105.
(9) Li, Z.; Sun, Q.; Yao, X. D.; Zhu, Z. H.; Lu, G. Q. *J. Mater. Chem.* **2012**, *22*, 22821.
(10) Han, C.; Li, Z.; Dou, S. *Chin. Sci. Bull.* **2014**, *59*, 2073.
(11) Han, C.; Li, Z.; Li, W. J.; Chou, S. L.; Dou, S. *J. Mater. Chem. A* **2014**, *2*, 11683.
(12) Liu, H. L.; Shi, X.; Xu, F. F.; Zhang, L. L.; Zhang, W. Q.; Chen, L. D.; Li, Q.; Uher, C.; Day, T.; Snyder, G. J. *Nat. Mater.* **2012**, *11*, 422.
(13) Slack, G. A. *Solid State Phys.* **1979**, *34*, 1.
(14) Kanishka, B.; He, J.; Ivan, D. B.; Wu, C.; Hogan, T. P.; Seidman, D. N.; Dravid, V. P.; Kanatzidis, M. G. *Nature* **2012**, *489*, 414.
(15) He, Y.; D, T.; Zhang, T. S.; Liu, H. L.; Shi, X.; Chen, L. D.; Snyder, G. J. *Adv. Mater.* **2014**, *26*, 3974.
(16) Mi, W. L.; Qiu, P. F.; Zhang, T. S.; Lv, Y. H.; Shi, X.; Chen, L. D. *Appl. Phys. Lett.* **2014**, *104*, 133903(1−5).
(17) Liu, H. L.; Yan, X.; Lu, P.; Shi, X.; Xu, F. F.; He, Y.; Tang, Y. S.; Bai, S. Q.; Zhang, W. Q.; Chen, L. D.; Lin, Y.; Shi, L.; Lin, H.; Gao, X. Y.; Zhang, X. M.; Chi, H.; Uher, C. *Adv. Mater.* **2013**, *25*, 6607.
(18) Ishiwata, S.; Shiomi, Y.; Lee, J. S.; Bahramy, M. S.; Suzuki, T.; Uchida, M.; Arita, R.; Taguchi, Y.; Tokura, Y. *Nat. Mater.* **2013**, *12*, 512.
(19) Hong, A. J.; Li, L.; Zhu, H. X.; Zhou, X. Y.; He, Q. Y.; Liu, W. S.; Yan, Z. B.; Liu, J. M.; Ren, Z. F. *Solid State Ionics* **2014**, *261*, 21.
(20) Fang, C. X.; Zhang, S.; Zuo, P. F.; Wei, W.; Jin, B. K.; Wu, J. Y.; Tian, Y. P. *J. Cryst. Growth* **2009**, *311*, 2345.
(21) Gao, Y. H.; Zheng, Z.; Tian, Y. P.; Zhang, Y. D.; Zhang, Y.; Eur, J. *Inorg. Chem.* **2011**, *27*, 4198.
(22) Perdew, J. P.; Burke, K.; Ernzerhof, M. *Phys. Rev. Lett.* **1996**, *77*, 3865.
(23) Delley, B. *J. Chem. Phys.* **1990**, *92*, 508.
(24) Delley, B. *J. Chem. Phys.* **2000**, *113*, 7756.
(25) Sun, Q.; Li, Z.; Searles, D. J.; Chen, Y.; Lu, G. Q.; Du, A. J. *J. Am. Chem. Soc.* **2013**, *135*, 8246.
(26) Frueh, A. J.; Czamanske, G. K.; Knight, C. H. *Z. Kristallogr.* **1957**, *108*, 389.
(27) Bikkulova, N. N.; Assylguzhina, G. N.; Skomorokhov, A. N.; Yadrovskii, E. L.; Beskrovnyi, A. I.; Stepanov, Y. M. *Bull. Russ. Acad. Sci.: Phys.* **2006**, *70*, 641.
(28) Baikulov, R. B.; Asadov, Y. G. *Inorg. Mater.* **2005**, *41*, 407.
(29) Chen, X. Q.; Li, Z.; Bai, Y.; Sun, Q.; Wang, L. Z.; Dou, S. X. *Chem.—Eur. J.* **2014**, DOI: 10.1002/chem.201405354.
(30) Xiong, J. Y.; Li, Z.; Chen, J.; Zhang, S. Q.; Wang, L. Z.; Dou, S. *ACS Appl. Mater. Interfaces* **2014**, *6*, 15712.
(31) Vanderputten, D.; Ohta, D.; Zanoni, R. *Mater. Sci. Forum* **1995**, *195*, 123.
(32) Riha, S. C.; Johnson, D. C.; Prieto, A. L. *J. Am. Chem. Soc.* **2011**, *133*, 1383.
(33) Domashevskaya, E. P.; Gorbachev, V. A.; Terekhov, V. A.; Kashkarov, V. M.; Panfilova, E. V.; Shchukarev, A. V. *J. Electron Spectrosc. Relat. Phenom.* **2001**, *114*, 901.